KeA1

CHINESE ROOTS
GLOBAL IMPACT

Contents lists available at ScienceDirect

Petroleum Science

journal homepage: www.keaipublishing.com/en/journals/petroleum-science



Original Paper

Multidimensional data-driven porous media reconstruction: Inversion from 1D/2D pore parameters to 3D real pores



Peng Chi ^{a, b}, Jian-Meng Sun ^{a, b}, Ran Zhang ^c, Wei-Chao Yan ^{d, e, f, *}, Huai-Min Dong ^{g, h}, Li-Kai Cui ^{h, i}, Rui-Kang Cui ^{a, b}, Xin Luo ^{a, b}

- ^a State Key Laboratory of Deep Oil and Gas, China University of Petroleum (East China), Qingdao, 266580, Shandong, China
- ^b School of Geosciences, China University of Petroleum (East China), Qingdao, 266580, Shandong, China
- ^c Geosteering & Logging Research Institute, Sinopec Matrix Corporation, Qingdao, 266003, Shandong, China
- ^d Frontiers Science Center for Deep Ocean Multispheres and Earth System, Key Lab of Submarine Geosciences and Prospecting Techniques, MOE and College of Marine Geosciences, Ocean University of China, Qingdao, 266100, Shandong, China
- ^e International Center for Submarine Geosciences and Geoengineering Computing (iGeoComp), Ocean University of China, Qingdao, 266100, Shandong, China
- f Laboratory for Marine Mineral Resources, Qingdao Marine Science and Technology Center, Qingdao, 266237, Shandong, China
- g School of Geological Engineering and Geomatics, Chang'an University, Xi'an, 710054, Shannxi, China
- ^h Xi'an Consin Energy Technology CO. LTD, Xi'an, 710100, Shannxi, China
- ¹ Institute of Unconventional Oil and Gas, Northeast Petroleum University, Daqing, 163318, Heilongjiang, China

ARTICLE INFO

Article history: Received 14 September 2024 Received in revised form 8 January 2025 Accepted 31 March 2025 Available online 2 April 2025

Edited by Meng-Jiao Zhou

Keywords:
3D digital rock
Pore network model
1D/2D pore parameters
Pore structure
Generative adversarial network

ABSTRACT

Subsurface rocks, as complex porous media, exhibit multiscale pore structures and intricate physical properties. Digital rock physics technology has become increasingly influential in the study of subsurface rock properties. Given the multiscale characteristics of rock pore structures, direct three-dimensional imaging at sub-micrometer and nanometer scales is typically infeasible. This study introduces a method for reconstructing porous media using multidimensional data, which combines one-dimensional pore structure parameters with two-dimensional images to reconstruct three-dimensional models. The pore network model (PNM) is stochastically reconstructed using one-dimensional parameters, and a generative adversarial network (GAN) is utilized to equip the PNM with pore morphologies derived from two-dimensional images. The digital rocks generated by this method possess excellent controllability. Using Berea sandstone and Grosmont carbonate samples, we performed digital rock reconstructions based on PNM extracted by the maximum ball algorithm and compared them with stochastically reconstructed PNM. Pore structure parameters, permeability, and formation factors were calculated. The results show that the generated samples exhibit good consistency with real samples in terms of pore morphology, pore structure, and physical properties. Furthermore, our method effectively supplements the micropores not captured in CT images, demonstrating its potential in multiscale carbonate samples. Thus, the proposed reconstruction method is promising for advancing porous media property research. © 2025 The Authors. Publishing services by Elsevier B.V. on behalf of KeAi Communications Co. Ltd. This is an open access article under the CC BY-NC-ND license (http://creativecommons.org/licenses/by-nc-nd/ 4.0/).

1. Introduction

Digital rock physics is a potent tool for examining the structural characteristics and physical properties of subsurface porous rocks. This non-destructive and efficient analytical technique not only complements laboratory-based rock physics experiments but also

facilitates rapid acquisition of pore structure data and simulation of underground conditions across various temperatures and pressures (Blunt et al., 2013; Fagbemi et al., 2018; Yang et al., 2021; Cai et al., 2022; Tian et al., 2023; Lv et al., 2024). Consequently, digital rock analysis has been extensively applied in fields such as oil and gas exploration and development, carbon capture and storage, hydrogeology, and geotechnical mechanics (Andhumoudine et al., 2021; Alpak and Saxena, 2023; Evstigneev et al., 2023; Mitchell et al., 2023; Zhang et al., 2023). The prevalent approaches for digital rock reconstruction include both physical experimental and

^{*} Corresponding author.

E-mail address: yanweichao@ouc.edu.cn (W.-C. Yan).

numerical reconstruction. Advances in three-dimensional (3D) scanning imaging have positioned techniques like X-ray CT and focused ion beam scanning electron microscopy (FIB-SEM) at the forefront of 3D rock reconstruction. These methods enable the capture of rock images across a spectrum of spatial scales (Karimpouli et al., 2020). However, a trade-off exists between resolution and field of view in 3D imaging. Micro-CT offers a broader field of view but lacks the capacity to resolve finer details (Chi et al., 2022). Whereas FIB-SEM, while yielding precise structural information, is limited to smaller physical dimensions (Dong et al., 2023). Thus, employing a combination of 3D imaging techniques in digital rock analysis ensures a thorough evaluation of pore structures.

The traditional numerical reconstruction method was initially designed to create idealized models of porous media for the analysis of fluid flow through pores (Zhu et al., 2019). Subsequently, techniques such as simulated annealing (Hazlett, 1997), sequential indicator simulation (Keehm et al., 2004), multi-point geostatistics (Okabe and Blunt, 2004), and Markov chain Monte Carlo methods (Wu et al., 2006) were employed, using two-dimensional (2D) images and experimental data, to reconstruct actual pore structures. Moreover, the expansion and application of pore network models have notably enhanced computational efficiency (Al-Kharusi and Blunt, 2007). By employing rock physics experimental data, the distributions of pores and throats can be determined, and the topological configuration of the pore network model (PNM) can be reconstructed with statistical information. Simulation of transport properties at the pore scale within the PNM facilitates the analysis of physical properties like capillary force. permeability, and resistivity (Golparvar et al., 2018; Wu et al., 2019; Qin et al., 2024; Cai et al., 2024). PNM more accurately represent the multiscale structure of rocks by integrating both macropores and micropores (Sun et al., 2021). Despite a remaining disparity in effectiveness compared to direct 3D imaging, numerical reconstruction methods provide significant efficiency and cost benefits (Tahmasebi et al., 2015; Wu et al., 2020).

In recent years, deep learning technology has been applied to 3D porous media modeling as a new numerical reconstruction method (Wang et al., 2021). Deep convolutional neural networks are primarily used for the 3D reconstruction of porous media, image super-resolution, and image transformation (Mosser et al., 2017; Buono et al., 2023; Zhu et al., 2024). For example, digital rock reconstruction can be achieved through the use of generative adversarial networks (GANs) and diffusion models, which allow for the imposition of conditional constraints to regulate the pore structure parameters within the reconstructed porous media (Chi et al., 2023; Luo et al., 2024). Post-training of these neural networks, a variety of digital rock types can be efficiently produced in

batch under specified conditions to meet numerical simulation demands. Super-resolution reconstruction techniques, such as SRCNN, SRGAN, and diffusion models, are employed to significantly improve the resolution of rock images, rendering finer details with clarity (Alqahtani et al., 2022; Ma et al., 2024). Super-resolution reconstruction can increase the resolution of rock images by several times, while also significantly increasing the amount of image data. Furthermore, image transformation techniques are pivotal for converting low-resolution images to high-resolution counterparts, often facilitating the integration of multi-source rock information, such as the transition between CT and scanning electron microscopy (SEM) images (Liu and Mukerji, 2022; Chi et al., 2024). Consequently, deep learning can effectively improve the precision and efficiency of digital rock reconstruction.

In current research, deep learning primarily reconstructs 3D digital rocks from an imaging perspective, rather than directly focusing on the topological aspects of pore structures. As a result, while the image quality of the generated digital rocks is commendable, there is a tendency for the outcomes to be overly uniform. That is, the generated data volumes are consistent with the training datasets, making it difficult to effectively expand the datasets. Firstly, it is not always feasible to have abundant 3D datasets for training, necessitating consideration of scenarios where 3D images are lacking (Tahmasebi and Sahimi, 2012; Hajizadeh et al., 2011). Secondly, generating digital rocks using only rock images without constraints from rock physics information will result in a lack of physical significance. Hence, the true virtue of numerical reconstruction methods lies in their ability to construct 3D digital rocks from limited pore structure data when comprehensive 3D data is not available.

This study addresses the challenge of lacking 3D images in practical applications by proposing a multidimensional data-driven approach to porous media reconstruction. The process integrates one-dimensional (1D) pore-throat distribution parameters with 2D rock images, enabling 3D digital rock reconstruction that incorporates multidimensional information. Our methodology comprises two stages: the stochastic generation of a PNM and the subsequent reconstruction of the digital rock. We used Berea sandstone and Grosmont carbonate samples, validating the digital rock reconstruction's precision through a comparison of the generation results of extracted and stochastically generated PNM. Postreconstruction, the accuracy of the reconstructed samples compared to actual samples was evaluated through visual observation, pore structure parameter computation, and simulation of pore transport. Finally, we presented an application example of reconstructing 3D digital rocks from 1D and 2D data in a carbonate sample, highlighting the promising prospects of our method.

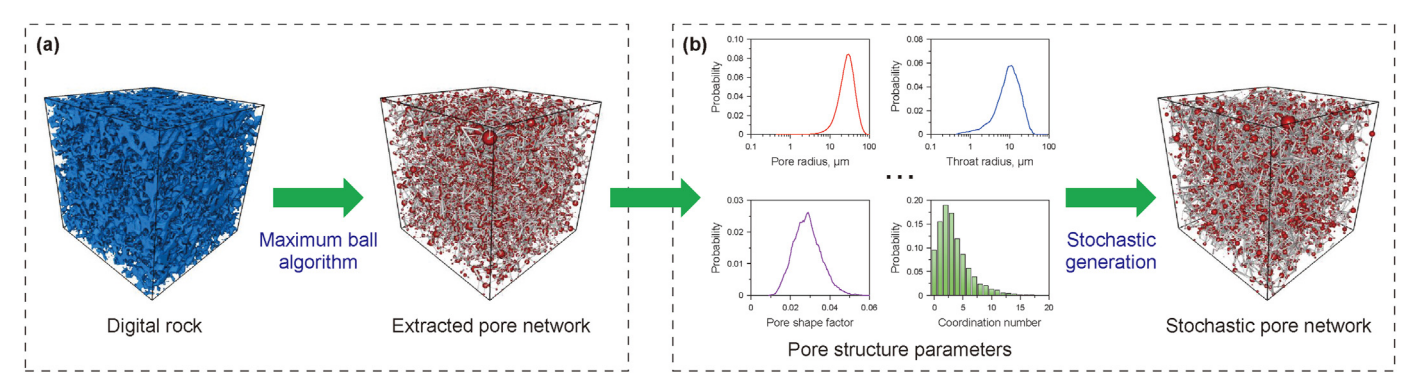


Fig. 1. Two methods for generating a PNM: (a) extraction from a digital rock, (b) stochastic generation using pore structure parameters.

2. Methodology

2.1. Pore network model extraction and stochastic reconstruction

The PNM is a simplified model that characterizes the spatial structure of pores and throats using spheres and tubes, which can be obtained either by extracting from digital rocks or by stochastic generation, as shown in Fig. 1. This study generates PNM using both methods to meet different application conditions. A common method for extracting PNM from existing digital rocks is the maximum ball algorithm (Dong and Blunt, 2009). This algorithm examines each pore voxel, expanding spherically to identify surrounding voxels. If no skeletal voxels are detected, the search radius expands until the rock skeleton is reached, ascertaining the maximum ball radius for that voxel. Upon completion of this process for all voxels, a comprehensive set of inscribed spheres is compiled. Any spheres with centers closer than the difference of their radii are eliminated to avoid overlap. The resulting nonredundant set of spheres defines the maximum sphere set, effectively mapping the pore space within the digital rock. A sorting algorithm is employed to order all elements in the maximum sphere set from largest to smallest by radius, and the spheres are divided into a series of subsets based on their radii. For each subset, a clustering algorithm is applied to the maximum spheres to determine whether they belong to pores or throats and to obtain the corresponding radii. After identifying pores and throats, various pore structure parameters can be obtained.

One-dimensional pore structure parameters can be used to construct a PNM inversely. Fig. 1(b) shows the process whereby parameters such as pore radius, throat radius, coordination number, and shape factor are utilized to stochastically generate a novel PNM (Dong et al., 2018). Initially, the size and porosity of the stochastically generated PNM must be determined. Following this, spheres representing pores are randomly introduced into the PNM, in accordance with the pore radius distribution curve, until the cumulative volume aligns with the pre-set porosity. Subsequently, topological information of the PNM is incorporated by considering the coordination number and throat distribution, with each pore assigned a specific weight as

$$P_i = \left(\frac{D_i - D_{\min}}{D_{\max} - D_{\min}}\right)^n \tag{1}$$

where P_i represents the ith pore, D_i is the diameter of the ith pore, D_{\min} and D_{\max} are the minimum and maximum pore diameters, respectively. n is the correlation factor, it indicates that when n > 0, larger throats are more likely to be connected to larger pores, whereas for n < 0, larger throats preferentially link to smaller pores.

In accordance with the coordination number distribution, each pore is connected to the closest neighboring pores, continuing this process until the last pore is connected. Upon completion of these connections, the weight of each throat is determined as

$$T_i = \frac{P_1 + P_2}{2} \tag{2}$$

where T_i represents the ith throat, while P_1 and P_2 denote the pore weights at the ends of the throat. The radius of each throat is determined based on these weights. Additionally, the shapes of the pores and throats are randomly assigned using a shape factor.

The pore structure parameters approximately follow a Weibull distribution. When the specific distribution of pore structure parameters cannot be completely enumerated, the Weibull distribution can be used for approximation as (Weibull, 1951)

$$f(x; \lambda, k) = \begin{cases} \frac{k}{\lambda} \left(\frac{x}{\lambda}\right) e^{-(x/\lambda)^k} & x \ge 0\\ 0 & x < 0 \end{cases}$$
 (3)

where x represents the continuous random variable, λ represents the scale parameter, and k represents the shape parameter.

For an existing digital rock, it is possible to carry out the two processes shown in Fig. 1. The initial method entails the extraction of the PNM and the computation of its structure parameters, subsequently followed by the stochastic generation of a novel PNM. In instances where digital rock images are absent, the procedure outlined in Fig. 1(b) can be exclusively executed, utilizing 1D parameters derived from experimental analyses to reconstruct the PNM. Each of these approaches can achieve the augmentation of PNM datasets.

2.2. Reconstructing real porous media from the pore network model

Constructing a PNM using only 1D parameters may result in an unrealistic representation of pore morphology. Hence, it is necessary to integrate 2D data to reconstruct realistic pore shapes. Given a digital rock model, its PNM can be extracted and then reconverted into a digital rock model. Fig. 2 shows this iterative process. By voxelizing, each pore and throat in the PNM is replaced with a 3D image voxel at the corresponding position. Deep learning techniques are then applied, using 2D pore images to transform the PNM into a true pore shape. This methodology is significant as it enables the conversion of a stochastically generated PNM into a form that reflects realistic pore morphologies, facilitating a 3D digital rock reconstruction that integrates 1D and 2D data.

Deep convolutional neural networks are frequently used for image fusion and style transfer tasks. This study utilizes a GAN model to integrate PNM with 2D rock images, facilitating the conversion of PNM into digital rocks (Goodfellow et al., 2014; Dahari et al., 2023). Fig. 3 shows the network architecture designed for this transformation, comprising a generator and a discriminator.

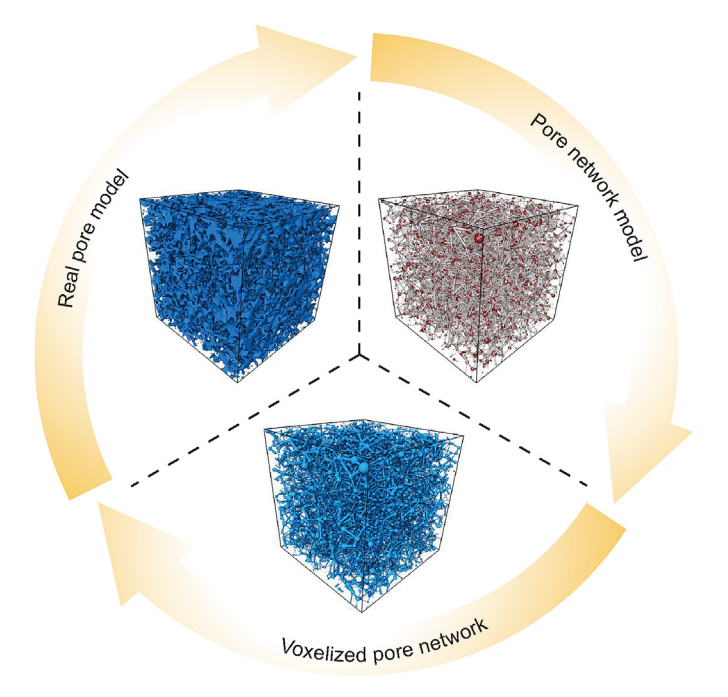


Fig. 2. Process of PNM extraction and digital rock reconstruction. Digital rock and PNM can be converted into each other within this cycle.

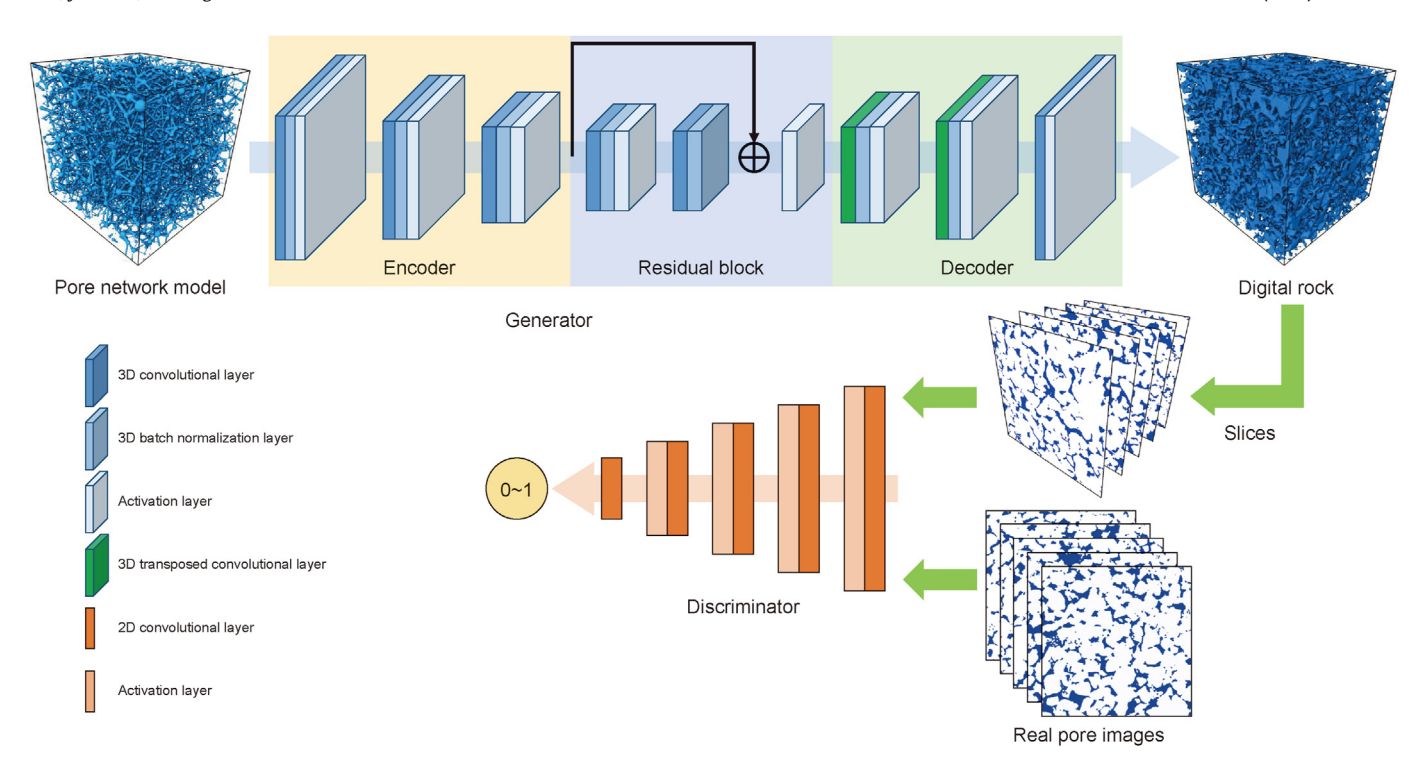


Fig. 3. Network architecture for converting a PNM into a digital rock.

Table 1The network architecture of the generator and discriminator.

	Layer	Kernel	Stride	Padding	Output shape
Generator	Input		_	_	$1 \times 64 \times 64 \times 64$
	1. Convolutional	3	1	1	$32\times 64\times 64\times 64$
	2. Convolutional	4	2	1	$64 \times 32 \times 32 \times 32$
	3. Convolutional	4	2	1	$128\times16\times16\times16$
	4. Residual	3	1	1	$128\times16\times16\times16$
	5. Transposed	4	2	1	$64\times32\times32\times32$
	6. Transposed	4	2	1	$32\times 64\times 64\times 64$
	7. Convolutional	3	1	1	$1\times 64\times 64\times 64$
Discriminator	Input	_	_	_	$1 \times 64 \times 64$
	1. Convolutional	4	2	1	64 imes 32 imes 32
	2. Convolutional	4	2	1	$128 \times 16 \times 16$
	3. Convolutional	4	2	1	$256 \times 8 \times 8$
	4. Convolutional	4	2	1	$512 \times 4 \times 4$
	5. Convolutional	4	2	0	$1 \times 1 \times 1$

The generator's function is to take the PNM as input and convert it into a digital rock, whereas the discriminator evaluates the consistency of the generated digital rock with actual two-dimensional pore images. During the training phase, both the generator and discriminator participate in the training, whereas only the generator is retained for testing or application. The generator is structured with an encoder, a decoder, and residual blocks: the encoder performs data downsampling through 3D convolutional layers, the decoder upsamples the data using 3D transposed convolutional layers, and the residual blocks are tasked with deep feature extraction. The discriminator is composed of a series of 2D convolutional layers, with inputs being real 2D pore images and slices of reconstructed digital rocks. Table 1 presents the network architecture of the generator and discriminator, showing that a PNM with a dimension of 64 is input into the generator, where the dimension is reduced to 16 after the encoder, and then restored to 64 after passing through the residual blocks and decoder.

During the training of deep neural networks, the Wasserstein

GAN with gradient penalty (WGAN-GP) framework has been implemented. This framework offers more stable gradient information by leveraging the continuous Wasserstein distance and employs gradient penalties to ensure the discriminator adheres to Lipschitz continuity. This approach effectively addresses the challenges of gradient explosion and vanishing gradients (Gulrajani et al., 2017). The generator loss utilized is defined as follows:

$$L_G = -E_{\boldsymbol{z} \sim p_{\boldsymbol{z}}(\boldsymbol{z})}[D(G(\boldsymbol{z}))] \tag{4}$$

The discriminator loss is defined as follows:

$$L_{D} = -E_{\mathbf{x} \sim p_{\text{data}}(\mathbf{x})}[D(\mathbf{x})] +E_{\mathbf{z} \sim p_{\mathbf{z}}(\mathbf{z})}[D(G(\mathbf{z}))] +\lambda E_{\mathbf{z} \sim p_{\mathbf{z}}(\mathbf{z})}[(\|\nabla D(\alpha \mathbf{x} + (1 - \alpha G(\mathbf{z})))\|_{2} - 1)^{2}]$$
(5)

To enable the generator to acquire the distribution characteristics of authentic data, the discriminator undergoes training five

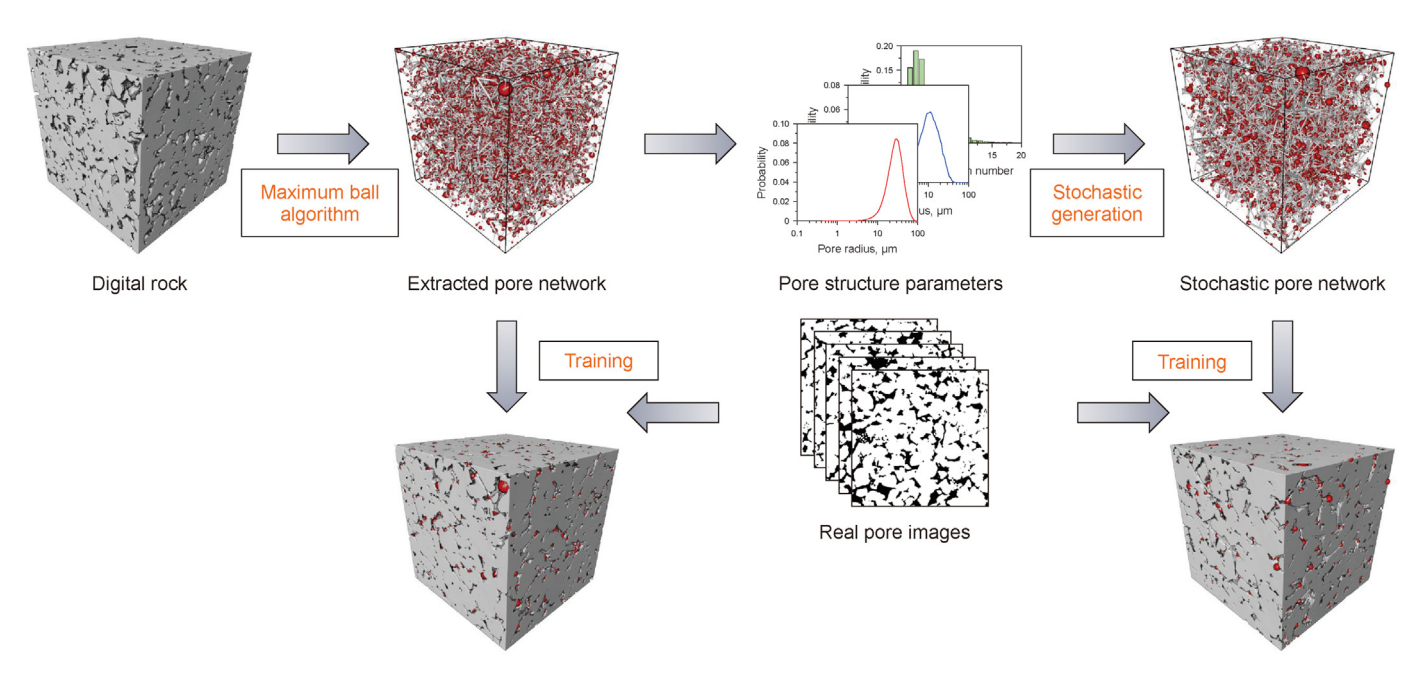


Fig. 4. Detailed process of PNM and digital rock reconstruction. The reconstruction under both extracted PNM and stochastic PNM is considered.

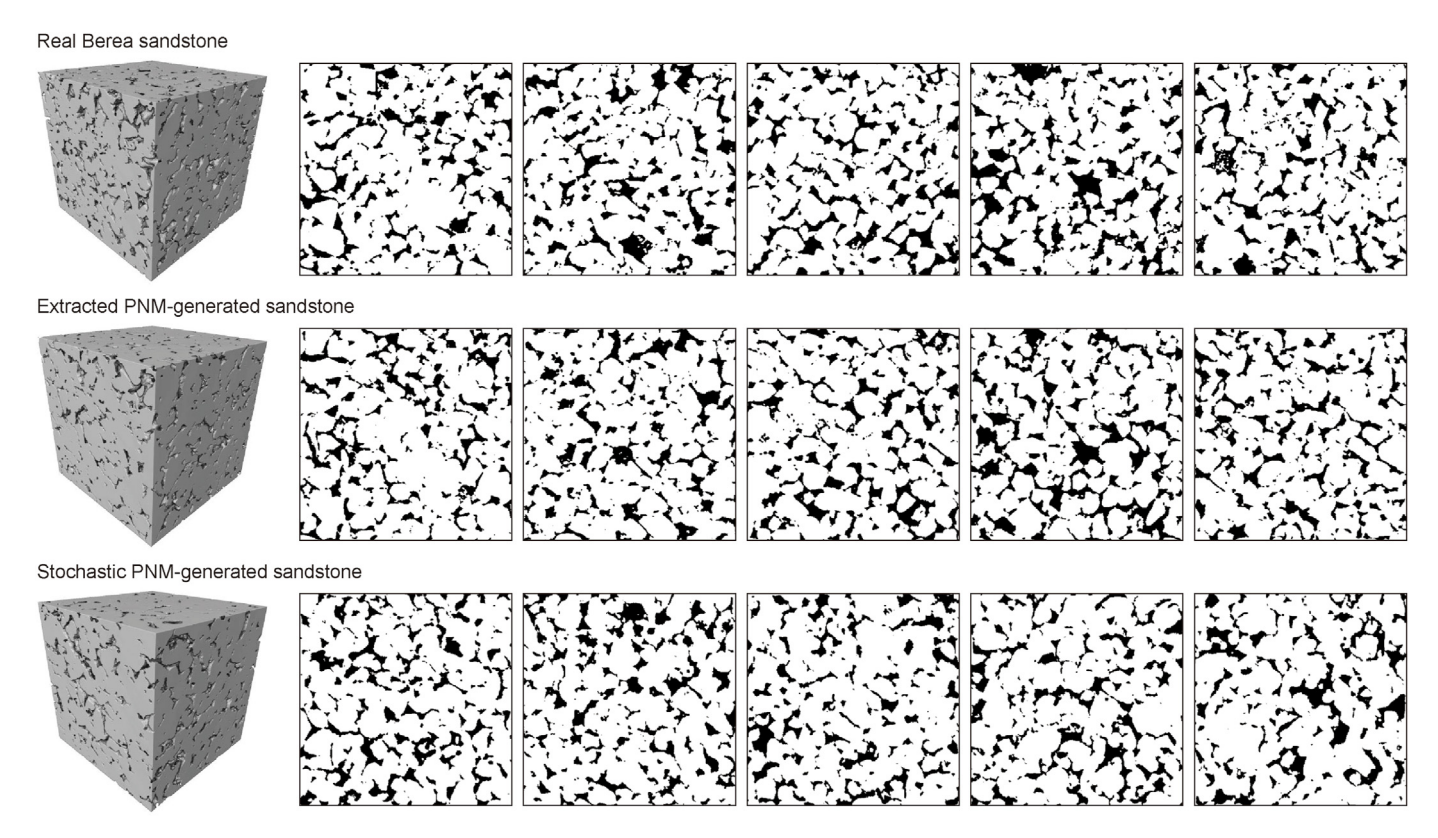


Fig. 5. Comparison of reconstruction results for Berea samples.

times for each training iteration of the generator. During the training phase, we conducted random sampling across the entire dataset with a batch size of 32. The training was executed using PyTorch on an NVIDIA GeForce RTX 3060 GPU, completing in approximately 15 h. The model employs a fully convolutional structure, and once trained, it can convert a PNM of any dimension

into realistic pores representative of that sample class. Consequently, by integrating the stochastic generation of PNM with the accurate depiction of real pore morphologies, PNM reconstructed from 1D pore structure parameters can be integrated with a limited number of 2D images to construct realistic pore models. This approach facilitates the reconstruction of 3D digital rocks from both

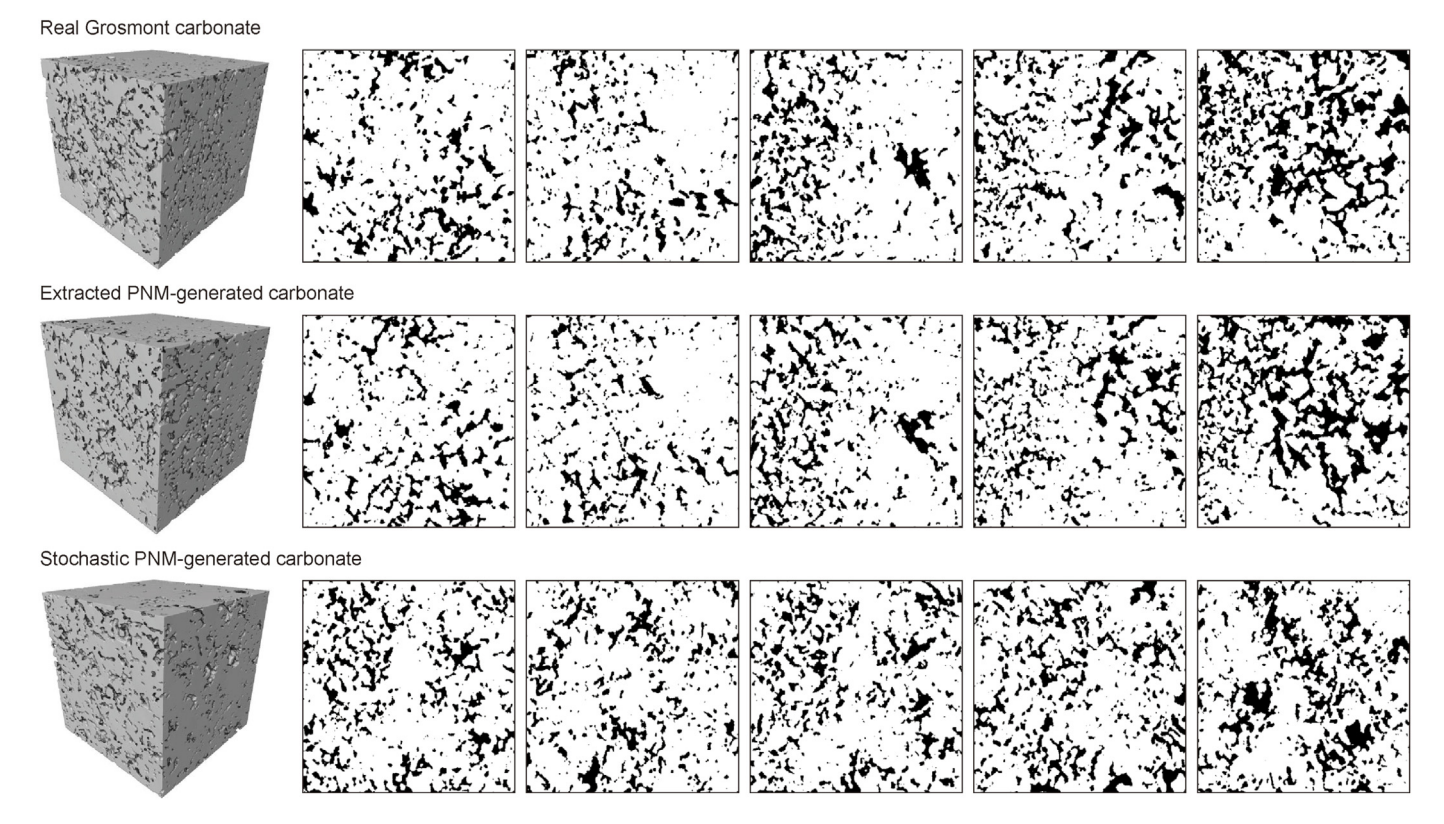


Fig. 6. Comparison of reconstruction results for Grosmont carbonate samples.

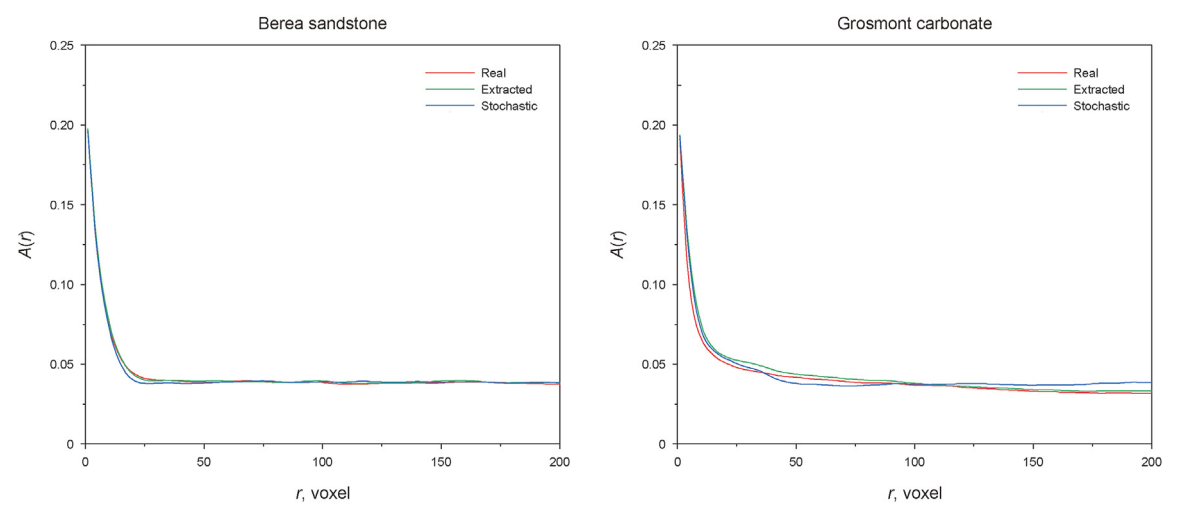


Fig. 7. Comparison of autocorrelation functions A(r) for Berea sandstone and Grosmont carbonate, where r stands for distance.

1D and 2D data.

3. Results and discussion

3.1. Evaluation of the effectiveness of digital rock reconstruction

To verify the accuracy of the stochastic PNM and reconstructed digital rocks separately, we have designed a series of experimental procedures as shown in Fig. 4. Initially, the PNM is extracted from the original digital rock using the maximum ball algorithm,

ensuring that the pores in the extracted PNM correspond one-to-one with those in the original digital rock. Subsequently, the 1D pore structure parameters of the extracted PNM are calculated, which are then utilized to generate a stochastic PNM. Following this, both sets of PNM are voxelized and fed into the GAN for training, using authentic 2D pore images as the ground truth for the discriminator, completing the fusion of the PNM with the real 2D images. Through this process, the reconstruction of 3D digital rocks from 1D and 2D data is achieved, and the accuracy of the reconstruction results is evaluated separately.

Berea sandstone and Grosmont carbonate were selected for the experimental dataset and subjected to the previously described procedure, yielding two sets of PNM and corresponding digital rock models (Andrä et al., 2013). The feasibility of the reconstruction method was initially assessed through image analysis. Fig. 5 presents the 3D volumes and 2D cross-sections of the actual Berea sandstone, extracted PNM-generated Berea sandstone, and stochastic PNM-generated Berea sandstone. The porosity measurements for these samples are 19.6%, 19.8%, and 19.6%, respectively.

The extracted PNM-generated sample has an identical PNM to the actual sample, resulting in very similar pore images. The pore sizes and positions of these two sets of images can be largely correlated one-to-one, and their connectivity is similar, indicating that the digital rock reconstructed from the PNM effectively restored the pore morphology of the actual Berea sandstone. This validation demonstrates the reliability of the digital rock reconstruction algorithm. Although the stochastic PNM is created by distributing pores of varying sizes randomly within a cubic framework, leading

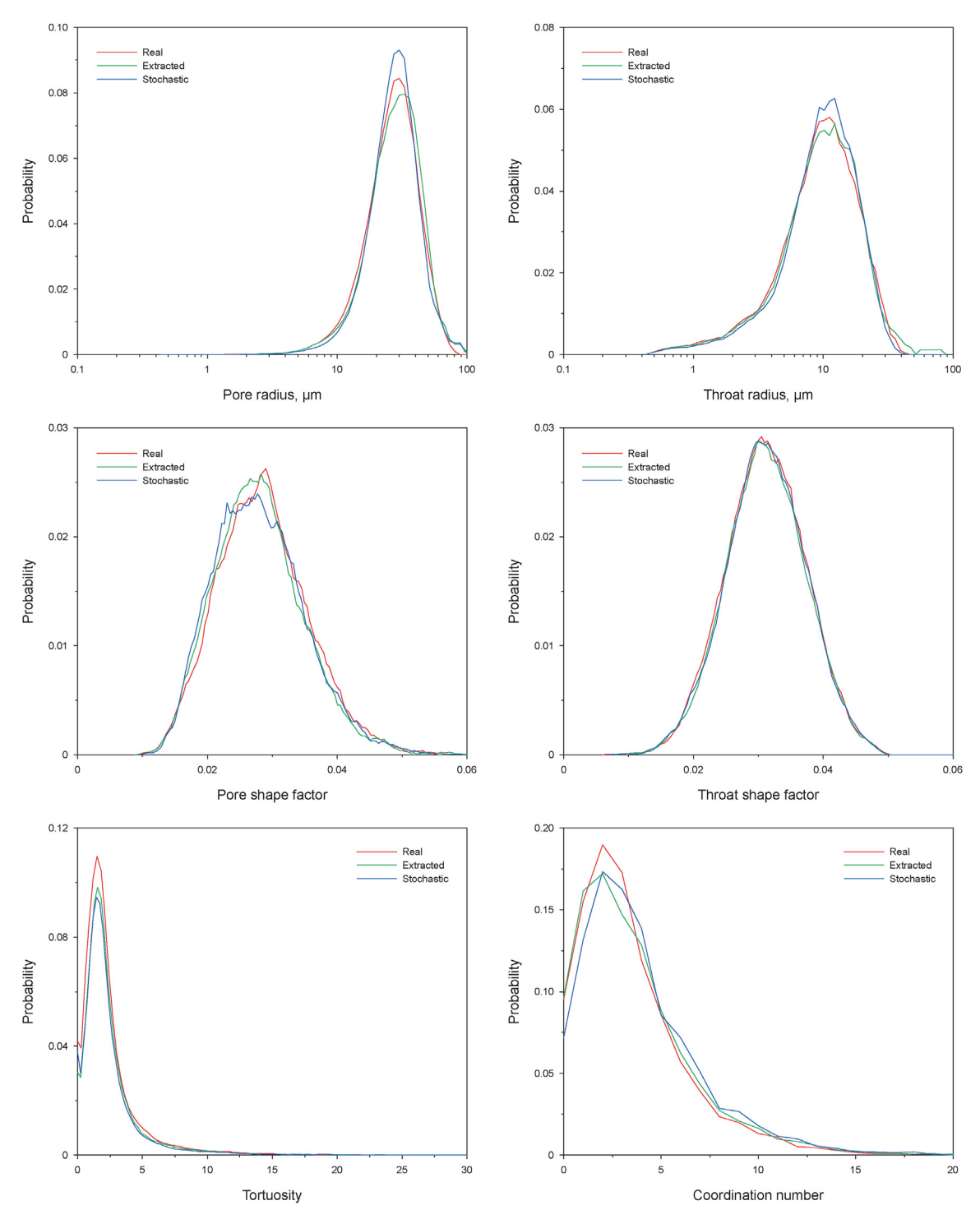


Fig. 8. Comparison of pore structure parameters for Berea sandstone.

to non-matching pore positions with the extracted PNM, the statistical distribution remains consistent. The digital rock generated from the stochastic PNM shows a high similarity to the actual Berea sample in terms of image, with consistent types of pores and grains, signifying the successful outcome of the stochastic PNM generation process.

The Grosmont carbonate samples underwent identical processing and comparison. Fig. 6 shows the 3D volumes and 2D cross-sections of the actual carbonate sample, the extracted PNM-

generated sample, and the stochastic PNM-generated sample. The porosities of the three samples are 19.1%, 19.4%, and 19.3%, respectively. In contrast to Berea sandstone, the Grosmont carbonate samples display significant heterogeneity, characterized by a non-uniform distribution of pores sizes. In the case of Grosmont carbonate samples, the extracted PNM-generated sample still maintains consistency in the distribution of pore size and position with the actual sample, showing a good correspondence and effectively restoring the pore morphology of the carbonate. Although the

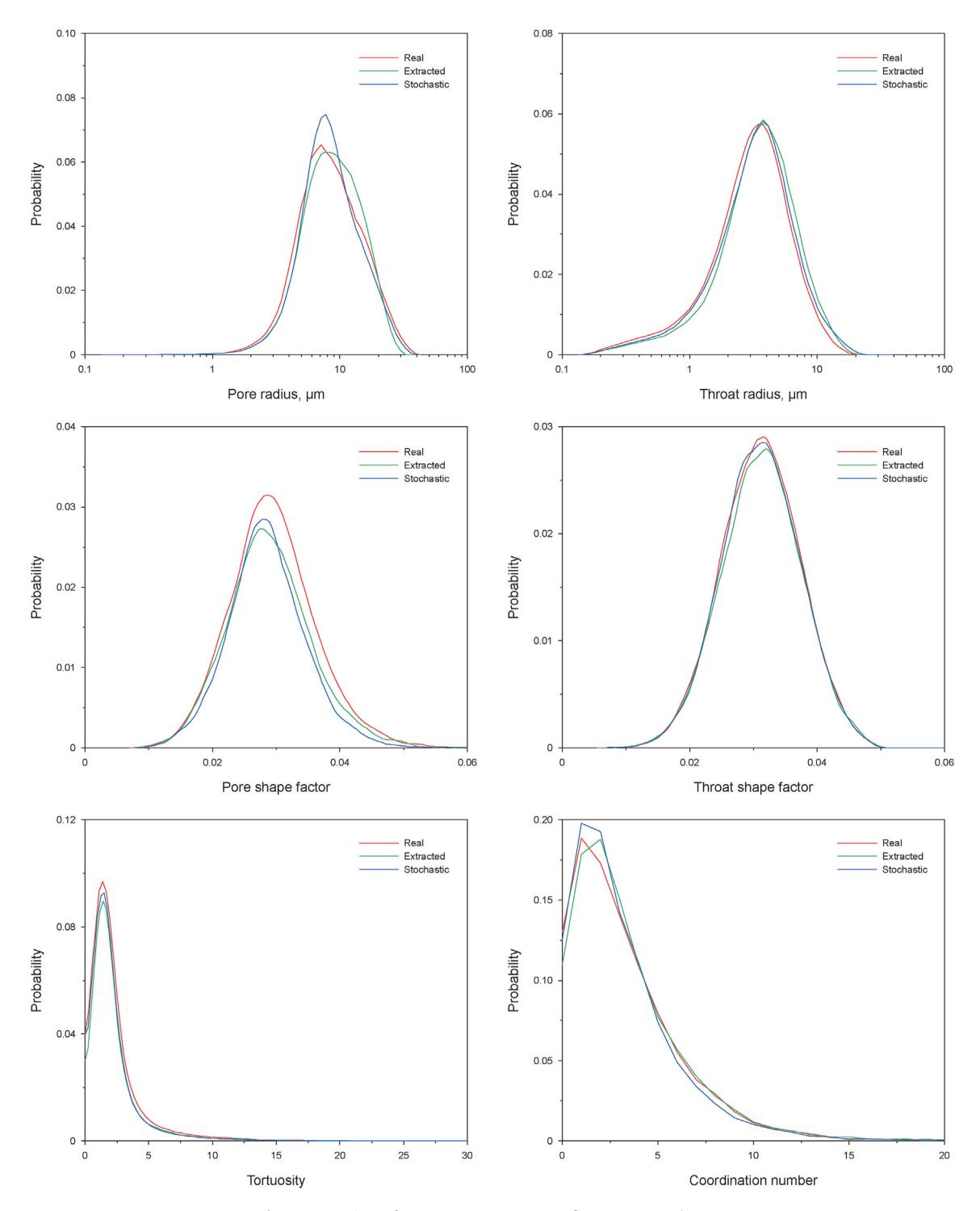


Fig. 9. Comparison of pore structure parameters for Grosmont carbonate.

stochastic PNM-generated sample does not precisely mirror the pore spatial distribution of the actual sample, it does reflect similar pore sizes and shapes. Consequently, the images of both sandstone and carbonate indicate that the PNM-derived samples accurately reflect pore sizes and position, indicating that the algorithm for generating digital rocks using PNM is reliable. Although the stochastic PNM-generated pore network cannot fully replicate the positions of pores of different sizes, the pore morphology in the generated images is similar to that of the actual samples.

Image observation only provides the similarity of the pores, but does not allow for a direct comparison of pore structure information, necessitating further comparison of pore structure parameters. The pore structure parameters of the generated digital rocks were statistically analyzed and compared with the actual samples. The autocorrelation function, which indicates the likelihood of two points at a distance r in a binary image both in pore space, is utilized to characterize the pore structure of the rock. Fig. 7 shows the autocorrelation functions of Berea sandstone and Grosmont carbonate, with the autocorrelation functions of the reconstructed samples being consistent with those of the actual samples. Figs. 8 and 9 present the calculation results of the pore structure parameters for Berea sandstone and Grosmont carbonate, respectively, comparing the distributions of pore radius, throat radius, pore shape factor, throat shape factor, tortuosity, and coordination number between the two types of samples. The sandstone samples exhibit larger average pore throat radius compared to carbonate samples. The range of pore structure parameters for both the actual and reconstructed samples derived from both extracted PNM and stochastic PNM is similar. Although the pore space distribution of the stochastic PNM does not completely match that of the actual samples, the pore types and their distribution ranges are consistent. Consequently, the digital rocks generated from the extracted PNM closely resemble the actual samples in terms of pore structure parameters, further demonstrating the effectiveness of the digital rock reconstruction method.

By simulating the transport properties of pores, the effectiveness of digital rock reconstruction can be verified. Permeability reflects the fluid flow capacity of porous media, while the formation factor reflects the electrical conductivity. The lattice Boltzmann method (LBM) and the finite element method (FEM) were utilized to simulate permeability and formation factor, respectively. LBM, based on the statistical theory of the Boltzmann equation, solves fluid flow problems by simulating the distribution of particles on the pore lattice (Chen et al., 1992; Yan et al., 2021). In the initial state of the 3D pore structure, the pores are saturated with a certain fluid. Under periodic boundary conditions, the same fluid is injected from one end of the model. By combining Darcy's law and LBM simulation, the absolute permeability of the digital rock in a certain direction can be calculated. FEM (Garboczi, 1998; Dong et al., 2022) determines the energy of the porous media by

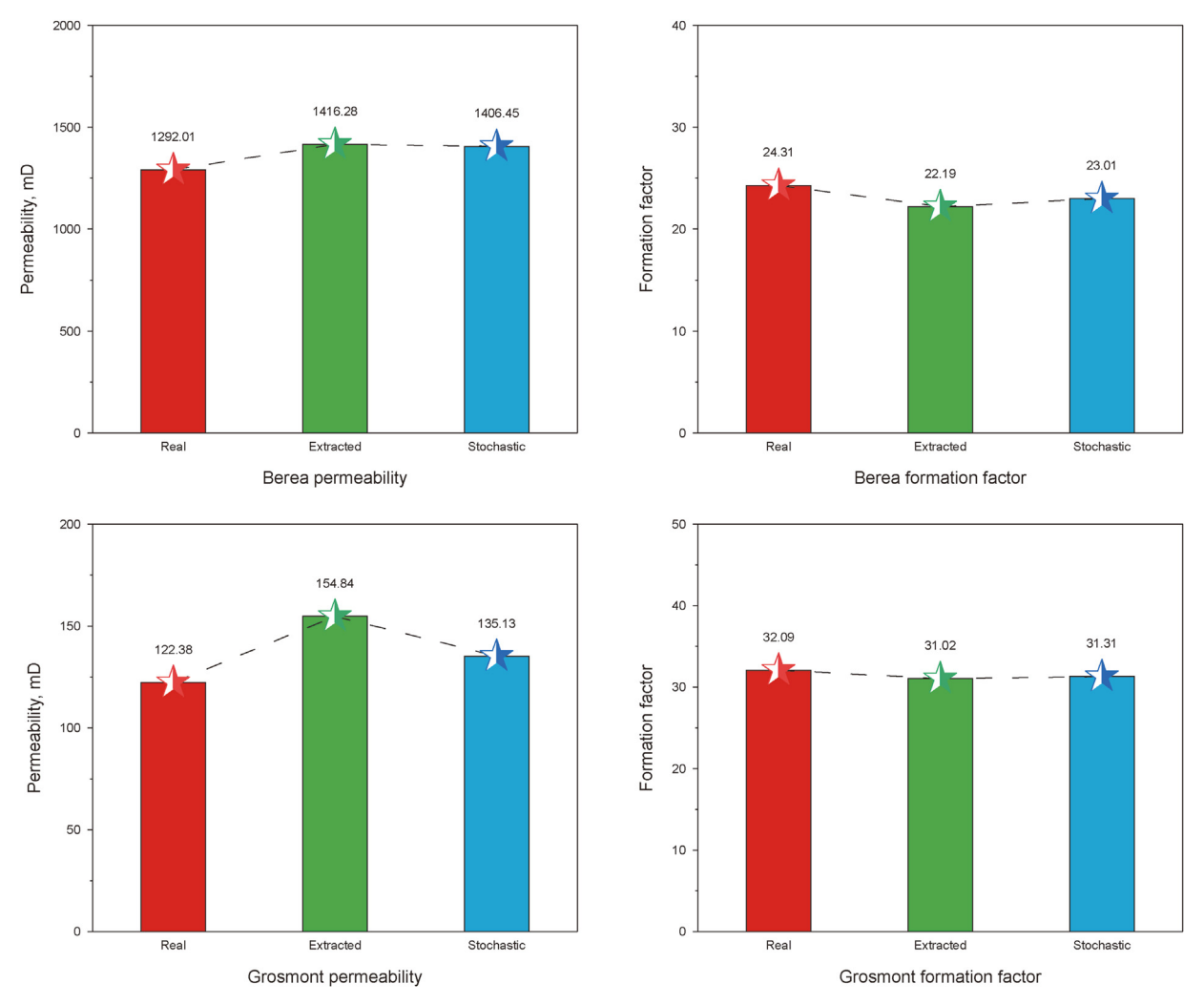


Fig. 10. Comparison of simulation results for permeability and formation factors of Berea sandstone and Grosmont carbonate.

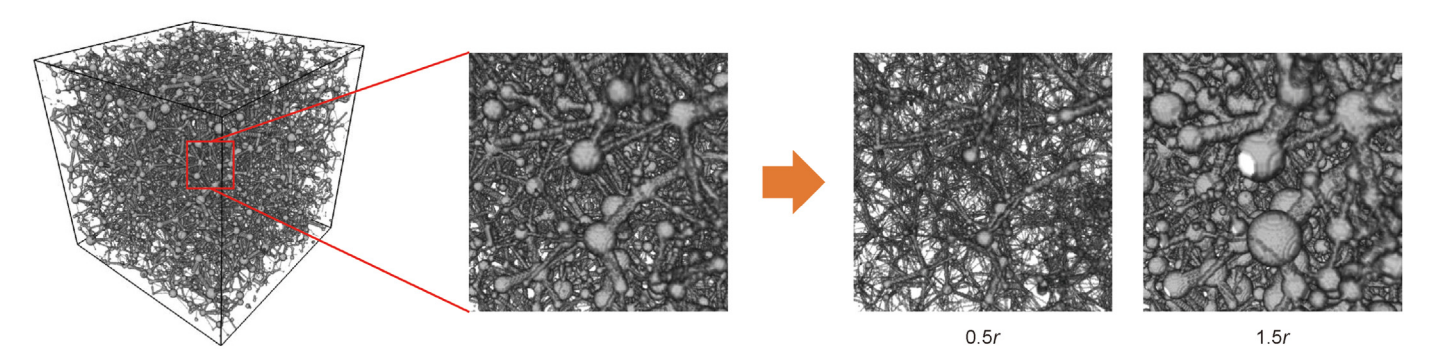


Fig. 11. Pore networks that has been voxelized after changing the parameters of the pore throat radius. Here, 0.5 and 1.5 represent the multiples of radius change.

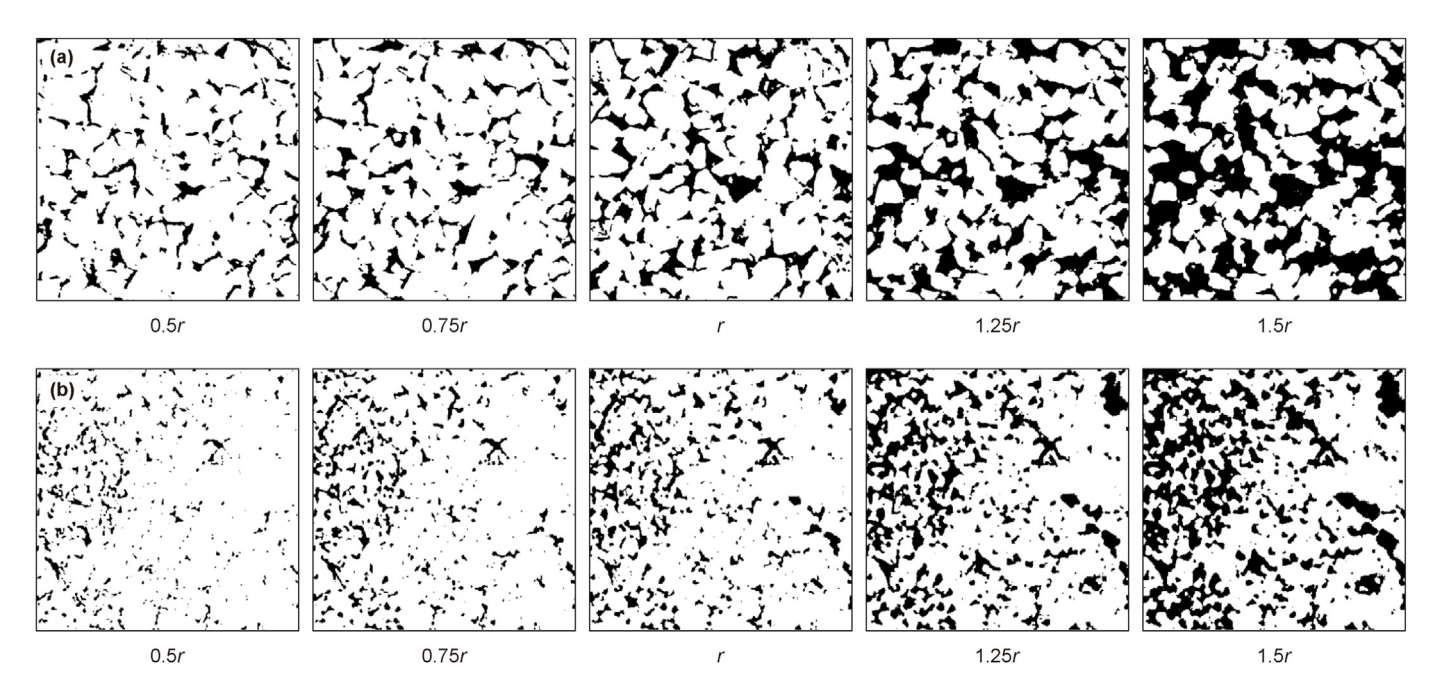


Fig. 12. Rock images generated after the PNM pore throat radius was changed by 0.5–1.5 times. (a) Berea sandstone and (b) Grosmont carbonate.

establishing an electric field across its extremities, with the voltage distribution across each voxel dictating the model's total energy. According to the principle of variation, the calculation of the voltage distribution can be transformed into a problem of finding the extreme value of the system's energy, ultimately determining the digital rock's effective electrical conductivity. The permeability and formation factor of Berea sandstone and Grosmont carbonate were calculated using both LBM and FEM. Fig. 10 shows a comparison of the numerical simulation results, with the permeability and formation factor of the original samples, extracted PNM-generated samples, and stochastic PNM-generated samples being close to each other. This indicates that the reconstructed digital rocks of Berea sandstone and carbonate possess the same physical properties as the actual samples, thus our digital rock reconstruction process is effective.

3.2. Effect of PNM parameters on digital rock reconstruction

We adjusted the PNM parameters to validate our approach and highlight its advantages over existing methods. While current studies show that 3D structures can be generated from random noise, these processes tend to be random and uncontrollable. A random porous medium generation method has limited utility in

the study of subsequent physical phenomena. Consequently, we modified PNM parameters to influence the resulting 3D pore structure. In this subsection, instead of retraining on Berea sandstone and carbonate, we used the neural network parameters trained in the previous subsection to ensure the controllability of the experiment. By keeping the neural network parameters constant, we controlled the generation of 3D digital rocks by adjusting the PNM's pore throat radius. This was achieved by systematically altering the radius and volume in the PNM parameters by a scaling factor. Fig. 11 shows the PNM after adjusting the original pore throat radius to 0.5 times and 1.5 times and voxelizing, from which a clear change in the size of the pores and throats can be observed, while the topological structure remains unchanged. Using the trained neural network parameters, the voxelized PNM was transformed into 3D digital rocks, with the PNM pore throat radius ranging from 0.5 to 1.5 times the original radius. Fig. 12 shows the cross-sections of the 3D structures generated from two sets of samples. As the PNM parameters change, the generated pore throat radii follow a similar trend. Since the PNM's topological structure remains constant, the position of the pores and throats is unchanged, with only their size varying. Thus, our PNM-based approach to generating 3D structures provides enhanced control compared to methods using random noise or 2D images.

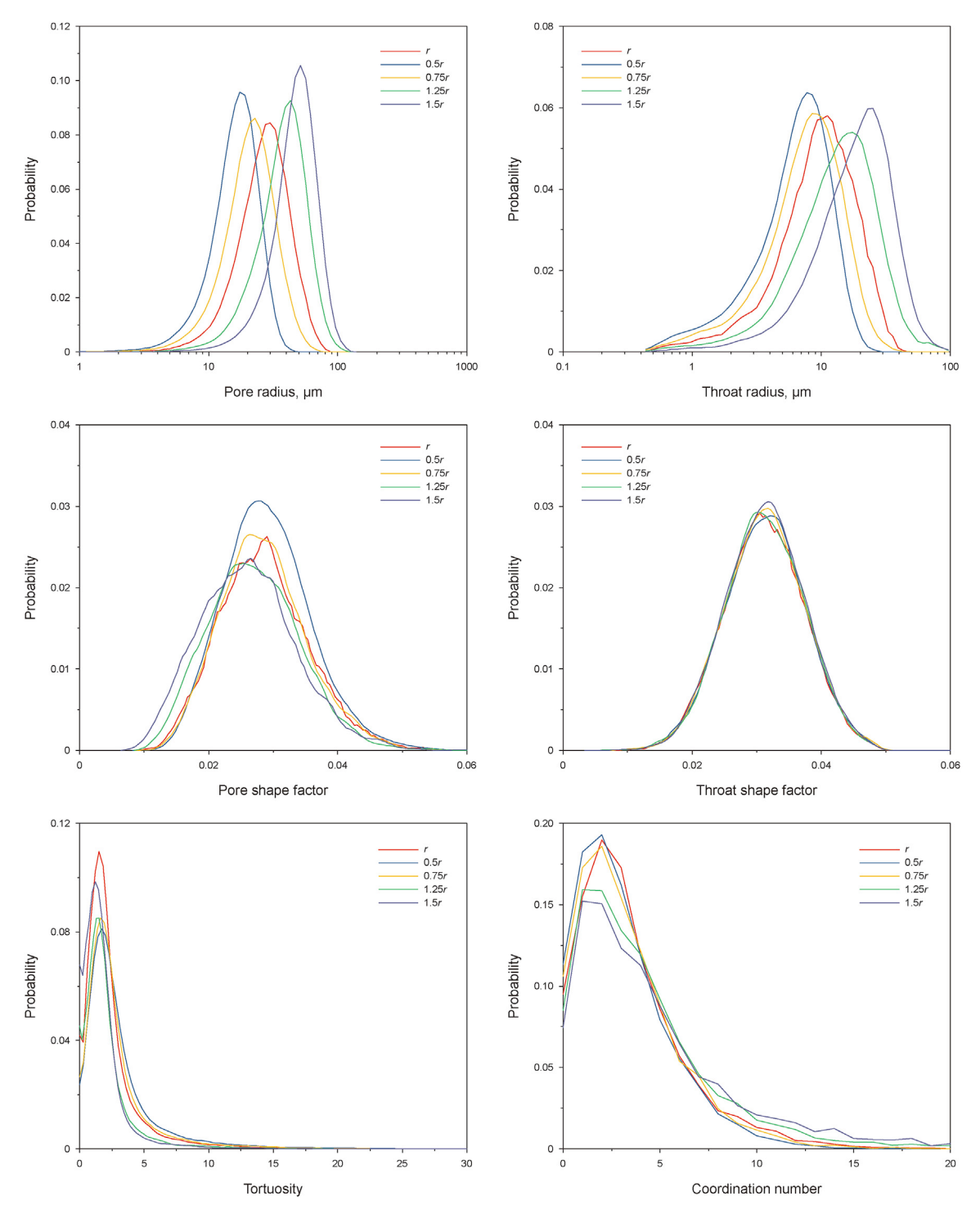


Fig. 13. Comparison of Berea pore structure parameters when the pore throat radii are varied.

We calculated the pore structure parameters of 3D digital rocks generated after adjusting the pore throat radius to quantitatively analyze the generation results. Figs. 13 and 14 present the calculation results of the pore structure parameters for Berea sandstone and Grosmont carbonate following PNM parameter adjustments. As the PNM pore throat radius changes, the calculated pore radius and throat radius both exhibit significant corresponding shifts. However, parameters including the pore shape factor, throat shape factor, tortuosity, and coordination number remained relatively

stable, suggesting that the pore morphology and topological structure are largely preserved despite changes in size. The effects of PNM parameter alterations on the digital rocks can be further explored through image processing and numerical simulation. Fig. 15 shows the influence of changes in pore throat parameters on porosity, permeability, and formation factor. The initial porosity and its variation for both sets of samples are similar. Permeability and formation factor align with the variations in pore throat parameters, consistent with the general principles of rock physics,

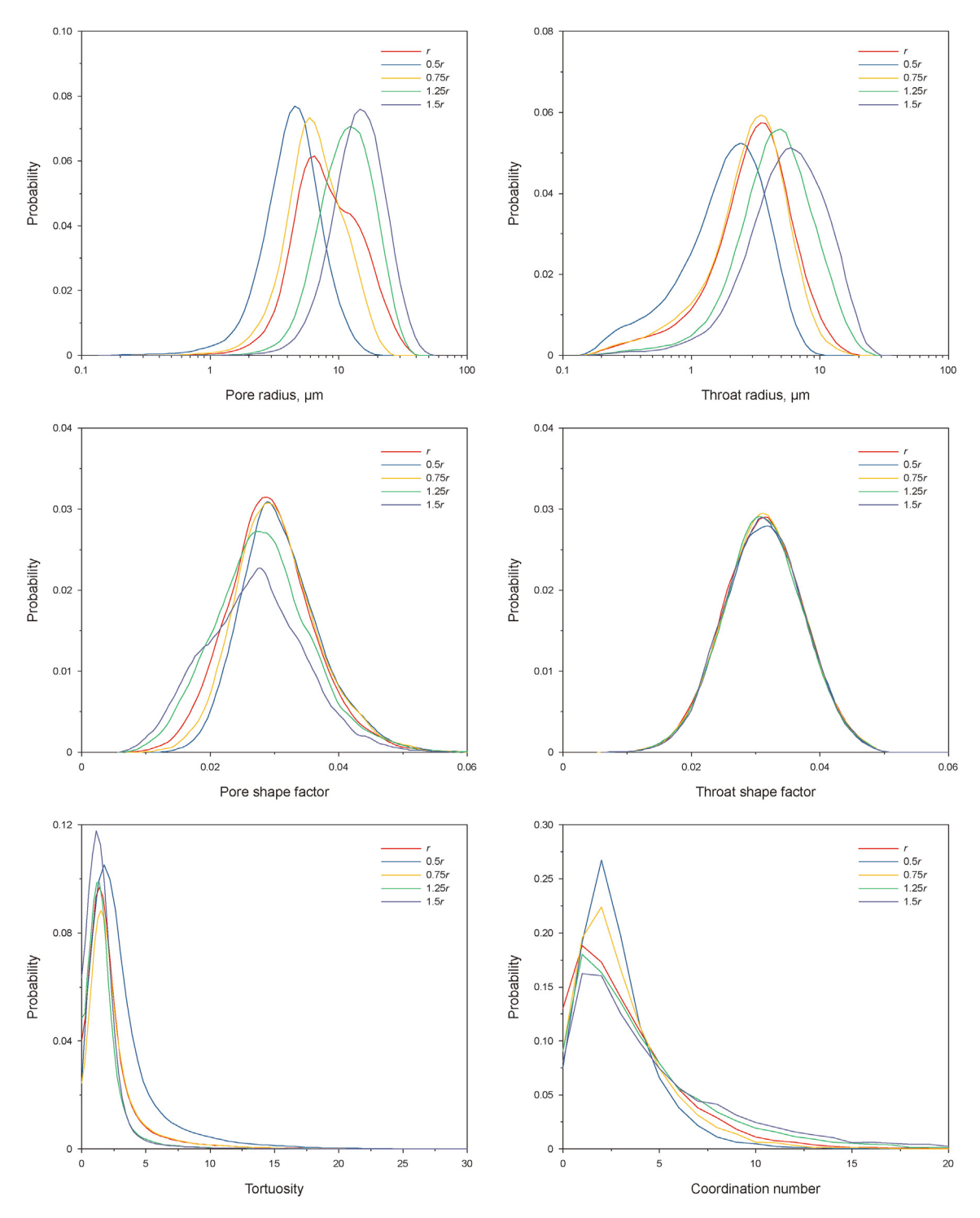
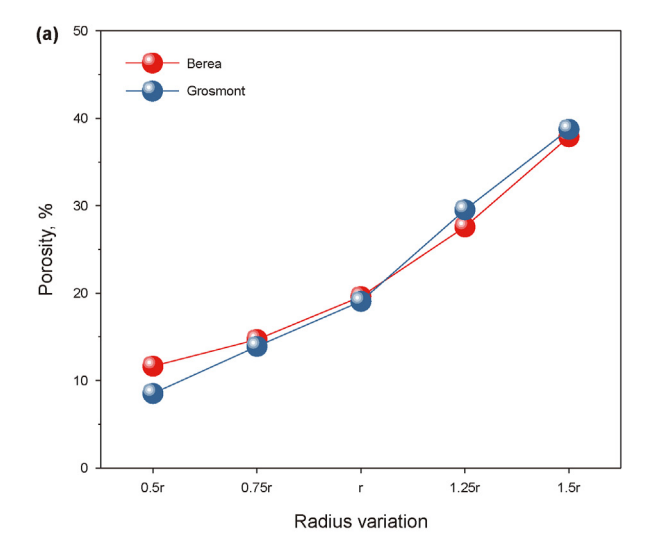


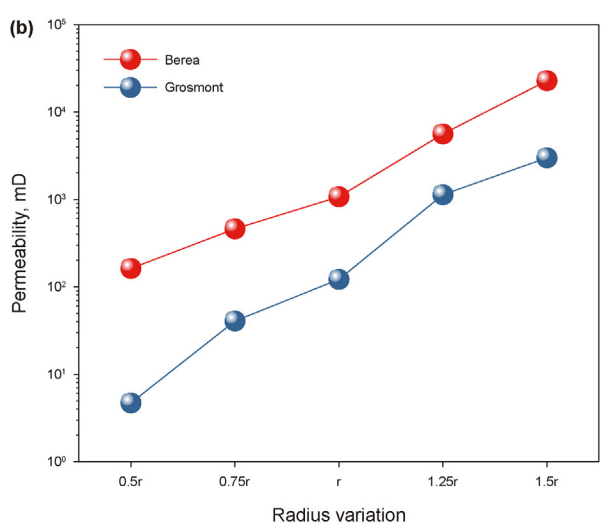
Fig. 14. Comparison of Grosmont carbonate pore structure parameters when the pore throat radii are varied.

without altering the topological structure. This indicates that the quantitative control over the pore structure of generated digital rocks can be effectively managed by modifying PNM parameters.

3.3. Application

Utilizing a carbonate sample from the Sichuan Basin in southwestern China, this section illustrates the application of our method in multidimensional data-driven digital rock modeling. Carbonate reservoirs typically exhibit multiscale characteristics with a wide range of pore sizes. Common testing methods, such as CT scanning, struggle to identify micropores, leading to poor connectivity in the reconstructed digital rocks. FIB-SEM, on the other hand, can only display a very small area, which is not representative. Therefore, multidimensional data can be integrated for multiscale digital rock reconstruction. Specifically, we used CT scan images as the basic framework, guided by pore structure parameters obtained from nuclear magnetic resonance (NMR) experiments





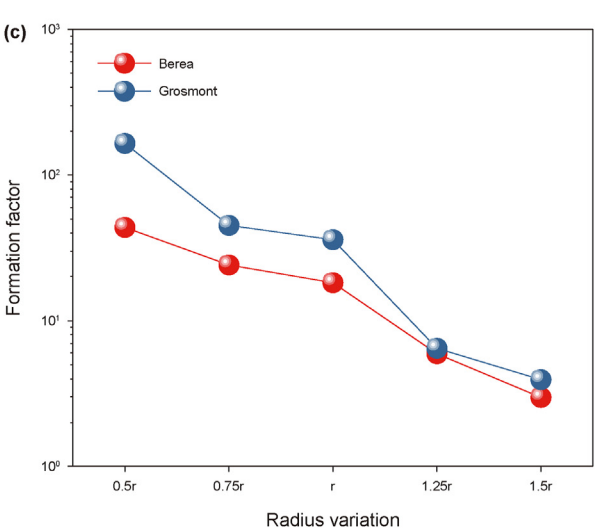


Fig. 15. Effects of pore throat radius changes on porosity, permeability, and formation factor.

and mercury intrusion capillary pressure (MICP) experiments, and supervised by high-resolution SEM images, to reconstruct digital rocks that reflect multiscale information.

Firstly, CT scanning, SEM testing, NMR experiments, and MICP

experiments are conducted on the carbonate sample. These are standard rock physics analysis methods, and the specific principles of the experiments will not be reiterated here. Fig. 16 shows SEM images and their binary processing, revealing the presence of micropores within the carbonate, but with a relatively low porosity. For micropore reconstruction, pore and throat distributions derived from NMR and MICP experiments were compared with those from CT scanning. Unidentified pores and throats at the current resolution were selected for stochastic PNM reconstruction. The pore radius distribution was determined as the difference between NMR and CT pore radius curves, while the throat radius distribution was the difference between MICP and CT throat radius curves. Other pore structure parameters that were difficult to obtain in experiments were approximated using the Weibull distribution and further obtained from 2D SEM images during GAN model training. The parameters used for the Weibull distribution are shown in Table 2. The voxelized PNM and binary SEM images were then utilized to train the GAN model for micropore reconstruction. Finally, the pores from CT scanning were superimposed with the reconstructed micropores to obtain a multiscale digital rock. Fig. 17 shows the digital rocks at these three stages, which are the pores obtained from CT scanning, the reconstructed micropores, and the total pores after superposition. The porosities of the samples are 4.6%, 3.3%, and 7.8%, respectively. The permeability for the reconstructed digital rock is 0.031 mD, while the corresponding experimental permeability measures 0.045 mD. The resolution of the CT images is 2 μ m, and the resolution of the SEM images is 0.5 μ m. A total of 60 training images were made from the SEM images used in the training, with a size of 512 \times 352 pixels. It is evident that the pores from CT scanning are mostly isolated, with larger pore sizes, while the connectivity of the reconstructed micropores has been significantly improved. The superposition of the two can represent pores of different sizes at the same time.

A comparison of the pore structure parameters from reconstructed digital rocks with experimental test results is presented. Fig. 18 shows these comparisons, with Fig. 18(a) depicting the CTscanned digital rock, the reconstructed micropore digital rock, and the superimposed multiscale digital rock. The superimposed multiscale digital rock exhibits pores of different scales. The portion of the radius distribution that exceeds the resolution is attributed to one-voxel pores. We apply a multiplier between 0 and 1 to the pore radius of these one-voxel pores during our calculations, which results in the calculated radii values exceeding the resolution. Applying this factor allows the calculated distribution of pore radii to conform to a normal distribution, aligning with the laws of pore distribution and enabling better comparison with experimental results such as NMR. Fig. 18(b) contrasts the pore radius distributions of the multiscale digital rock with those derived from NMR experiments, revealing congruence. Fig. 18(c) presents a comparison of the throat radius distribution between the multiscale digital rock and the MICP experiments, with both showing consistent distribution ranges. We also conducted a comparison of the throat radius distribution obtained from the capillary pressure conversion using PNM simulation. The throat radius obtained from MICP represents the pore volume controlled by throats of that size, and we approximate this volume fraction as the proportion of the throats. Consequently, our reconstruction method is capable of effectively integrating 1D pore-throat parameters with 2D SEM images, and by superimposing these with 3D CT data to produce a 3D digital rock that combines multidimensional data.

3.4. Discussion

We established a correlation between PNM and actual pores using image processing techniques, enabling mutual

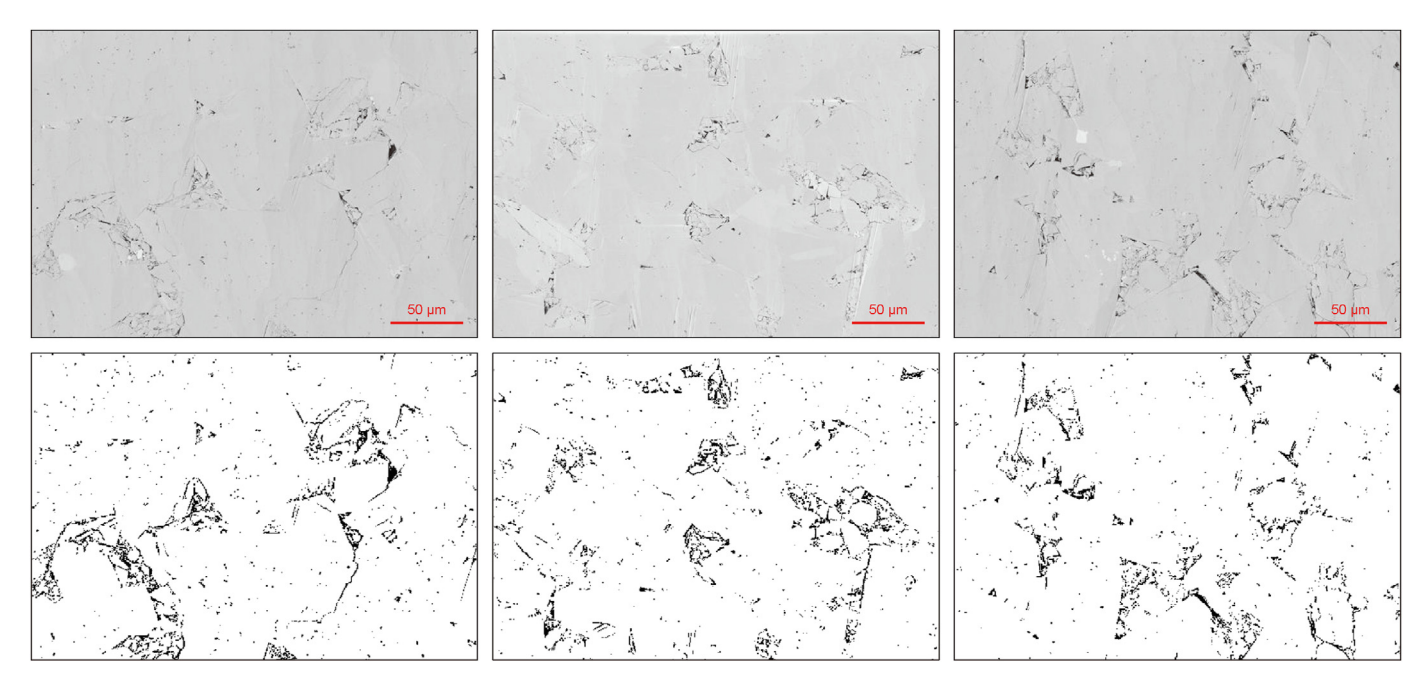


Fig. 16. SEM images of carbonate reservoir sample and the segmented pores.

Table 2Parameters of the Weibull distribution used in the generation of stochastic PNM.

Parameters	Minimum	Maximum	λ	k
Coordination number Pore shape factor Throat shape factor	0	50	0.11	1.2
	0.01	0.07	0.05	3.5
	0.01	0.06	0.03	2.7

transformation between the two. The experimental procedures designed involve reconstructing digital rocks from both extracted PNM and stochastic PNM, fully validating the effectiveness of our method. Visual assessments reveal that the digital rocks reconstructed from the extracted PNM closely resemble actual samples,

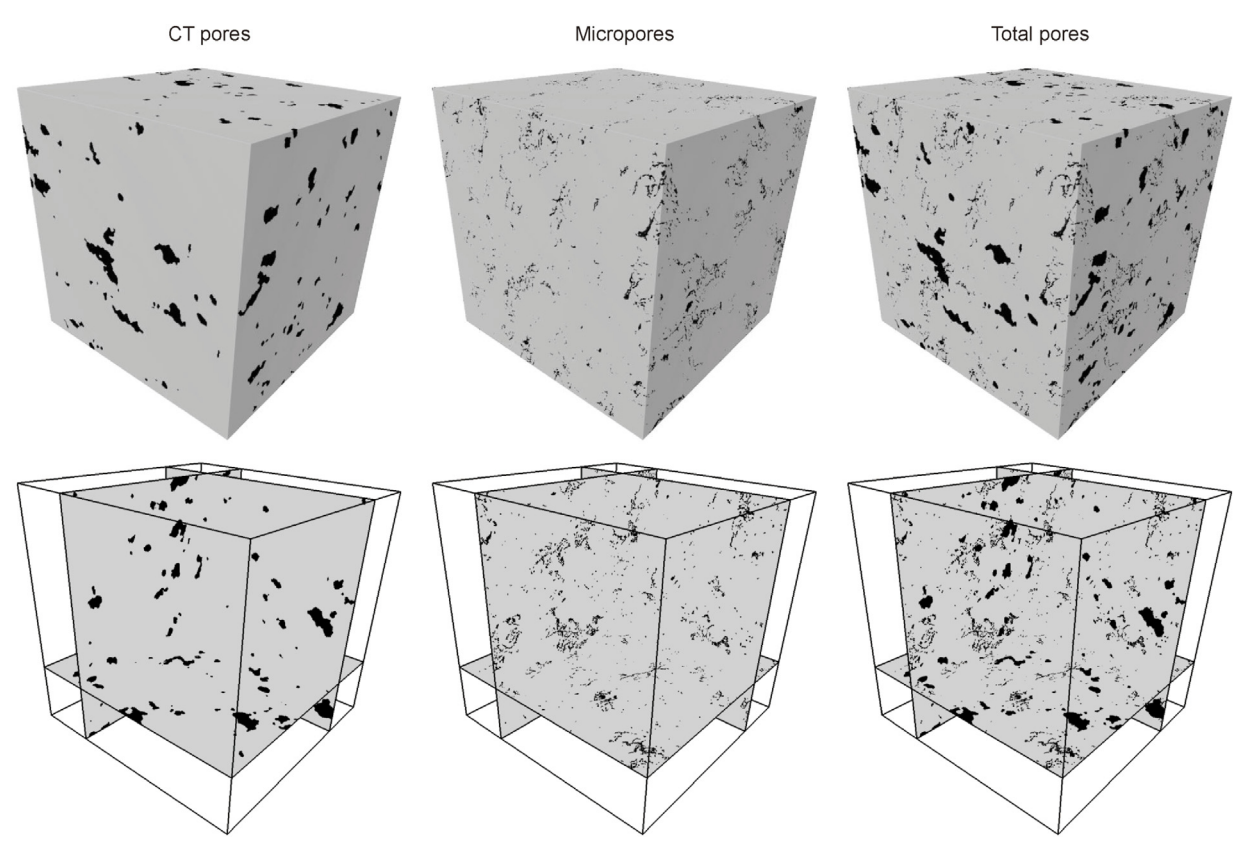
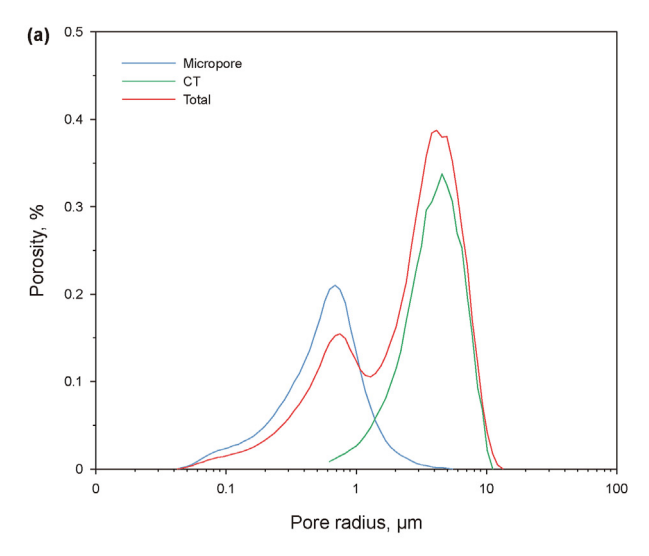


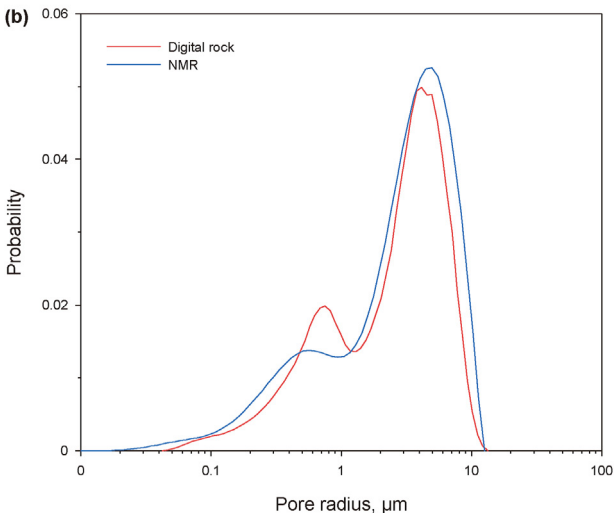
Fig. 17. Reconstructed 3D digital rocks and slices, derived from CT scanning, micropore reconstruction, and dual-scale pore superposition.

confirming the accuracy of our approach. Statistical analyses and numerical simulations demonstrate that the pore structure parameters and transport properties of the digital rocks reconstructed by these methods are very similar. Typically, in practical applications, the PNM is reconstructed using stochastic method. We illustrate a practical application with a case study detailing the 3D reconstruction process using experimental 1D parameters and 2D imaging. In this process, the sizes of pores and throats are derived from experiments, while other parameters that are difficult to obtain are replaced by the Weibull distribution. Subsequently, the real pore morphology is gradually obtained using 2D images in the training of GAN. This method enables the quantitative adjustment of pore structures in digital rock generation, enhancing the controllability of the modeling process. In this case study, we also performed CT scanning, so the reconstruction was defined as the part not identifiable by CT images, and then the CT digital rock was superimposed with the reconstructed micropore digital rock. The total pore distribution in the superimposed sample matches well with experimental data, indicating that our method effectively complements the identification of micropores not discernible by CT scans. In the 3D reconstruction, reconstructing the PNM is a prerequisite, with its pore and throat distribution being dictated by and aligned with the 1D data. Furthermore, the 2D data must align with the PNM's pore and throat distribution range; otherwise, the reconstruction technique becomes inapplicable. Our method enables the reconstruction of 3D porous media from 1D and 2D data, and it can stably control the size of the pores and throats in 3D reconstruction without altering the topological structure. This characteristic allows for the efficient construction of databases with different pore structures of porous media, which holds great promise for further analysis of the effects of pore throat structures on rock physical properties. It is important to note that the method's effectiveness in rocks exhibiting strong heterogeneity or anisotropy is not satisfactory, representing a challenge that requires attention in our future work.

4. Conclusion

This study introduces an efficient method for reconstructing 3D porous media using 1D and 2D data. It encompasses the reconstruction of the PNM from 1D data and the subsequent generation of digital rocks from the PNM using 2D images. The stochastic reconstruction method employs 1D pore structure parameters to produce a 3D PNM, serving as input for training a GAN. The GAN takes the voxelized pore network as input for the generator and real 2D images as true input for the discriminator, producing digital rocks with consistent pore distribution. The method was exemplified using Berea sandstone and Grosmont carbonate samples. where digital rock reconstruction was performed using PNM extracted by the maximum ball algorithm and stochastic PNM. The generated 3D digital rocks align with the 1D pore structure parameters and the 2D image pore morphologies, ensuring a high degree of realism. Simulations of permeability and conductivity were undertaken for the actual samples and samples reconstructed by the two methods, validating the precision of our approach. Our method exhibits superior controllability in the generation of digital rocks. It was extended to a carbonate sample with a multiscale pore structure, enabling the reconstruction of micropores undetectable by CT scanning and their integration with macropores to create a multiscale digital rock. Hence, our method enables the reconstruction of 3D porous media from 1D and 2D data, showing potential applications in the study of the micro-mechanisms of unconventional oil and gas reservoirs, as well as in the analysis of complex porous materials.





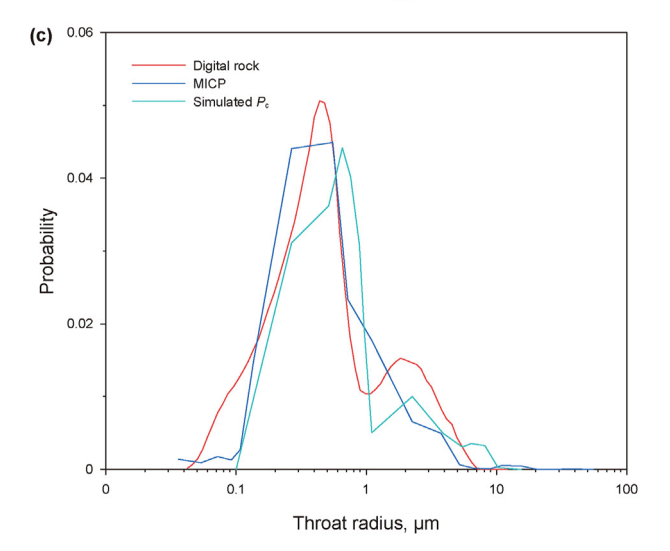


Fig. 18. Pore structure parameters of reconstructed multiscale digital rocks. **(a)** Comparison of CT pores, reconstructed micropores, and total pores in digital rocks. **(b)** Comparison of pore radius distribution between digital rock and NMR. **(c)** Comparison of throat radius distribution between digital rock, MICP, and simulated capillary pressure (P_c) .

CRediT authorship contribution statement

Peng Chi: Writing — original draft, Validation, Methodology, Investigation, Formal analysis, Data curation, Conceptualization. **Jian-Meng Sun:** Writing — review & editing, Visualization, Software, Funding acquisition, Data curation. **Ran Zhang:** Writing — original draft, Methodology, Investigation, Data curation. **Wei-Chao Yan:** Writing — review & editing, Supervision, Project administration, Funding acquisition, Data curation. **Huai-Min Dong:** Writing — review & editing, Investigation. **Li-Kai Cui:** Writing — review & editing, Investigation, Formal analysis. **Rui-Kang Cui:** Writing — review & editing, Validation, Formal analysis. **Xin Luo:** Writing — review & editing, Investigation, Data curation.

Declaration of competing interest

The authors declare that they have no known competing financial interests or personal relationships that could have appeared to influence the work reported in this paper.

Acknowledgments

This work was supported by the Shandong Provincial Natural Science Foundation (ZR2024MD116), National Natural Science Foundation of China (Grant Nos. 42174143, 42004098), and Technology Innovation Leading Program of Shaanxi (No. 2024 ZC-YYDP-27).

References

- Al-Kharusi, A.S., Blunt, M.J., 2007. Network extraction from sandstone and carbonate pore space images. J. Petrol. Sci. Eng. 56 (4), 219–231. https://doi.org/10.1016/j.petrol.2006.09.003.
- Alpak, F.O., Saxena, N., 2023. An accelerated process-based method for the accurate computation of relative permeability from direct simulations of two-phase flow on micro-computed tomography images of porous media. J. Petrol. Sci. Eng. 220, 111095. https://doi.org/10.1016/j.petrol.2022.111095.
- Alqahtani, N.J., Niu, Y., Wang, Y.D., Chung, T., Lanetc, Z., Zhuravljov, A., Armstrong, R.T., Mostaghimi, P., 2022. Super-resolved segmentation of X-ray images of carbonate rocks using deep learning. Transport Porous Media 143 (2), 497–525. https://doi.org/10.1007/s11242-022-01781-9.
- Andhumoudine, Å.B., Nie, X., Zhou, Q., Yu, J., Kane, O.I., Jin, L., Djaroun, R.R., 2021. Investigation of coal elastic properties based on digital core technology and finite element method. Adv. Geo-Energy Res. 5 (1), 53–63. https://doi.org/10.46690/ager.2021.01.06.
- Andrä, H., Combaret, N., Dvorkin, J., Glatt, E., Han, J., Kabel, M., Zhan, X., 2013. Digital rock physics benchmarks—Part I: imaging and segmentation. Comput. Geosci. 50, 25–32. https://doi.org/10.1016/j.cageo.2012.09.005.
- Blunt, M.J., Bijeljic, B., Dong, H., Gharbi, O., Iglauer, S., Mostaghimi, P., Paluszny, A., Pentland, C., 2013. Pore-scale imaging and modelling. Adv. Water Resour. 51, 197–216. https://doi.org/10.1016/j.advwatres.2012.03.003.
- Buono, G., Caliro, S., Macedonio, G., Allocca, V., Gamba, F., Pappalardo, L., 2023. Exploring microstructure and petrophysical properties of microporous volcanic rocks through 3D multiscale and super-resolution imaging. Sci. Rep. 13 (1), 6651. https://doi.org/10.1038/s41598-023-33687-x.
- Cai, J., Jiao, X., Wang, H., Wu, H., Xia, Y., 2024. Multiphase fluid-rock interactions and flow behaviors in shale nanopores: a comprehensive review. Earth Sci. Rev. 257, 104884. https://doi.org/10.1016/j.earscirev.2024.104884.
- Cai, J., Zhao, L., Zhang, F., Wei, W., 2022. Advances in multiscale rock physics for unconventional reservoirs. Adv. Geo-Energy Res. 6 (4), 271–275. https:// doi.org/10.46690/ager.2022.04.01.
- Chen, H., Chen, S., Matthaeus, W.H., 1992. Recovery of the Navier-Stokes equations using a lattice-gas Boltzmann method. Phys. Rev. A 45 (8), R5339. https://doi.org/10.1103/physreva.45.r5339.
- Chi, P., Sun, J., Luo, X., Cui, R., Dong, H., 2023. Reconstruction of 3D digital rocks with controllable porosity using CVAE-GAN. Geoenergy Sci. Eng. 230, 212264. https://doi.org/10.1016/j.geoen.2023.212264.
- Chi, P., Sun, J., Wang, Z., Ju, R., Wei, B., Duan, Y., 2022. Simulation of flow characteristics and development of permeability model in fractured-vuggy carbonate reservoir. J. Petrol. Sci. Eng. 219, 111098. https://doi.org/10.1016/j.petrol.2022.111098.
- Chi, P., Sun, J., Yan, W., Luo, X., 2024. Multiscale fusion of tight sandstone digital rocks using attention-guided generative adversarial network. Mar. Petrol. Geol. 160, 106647. https://doi.org/10.1016/j.marpetgeo.2023.106647.

Dahari, A., Kench, S., Squires, I., Cooper, S.J., 2023. Fusion of complementary 2D and 3D mesostructural datasets using generative adversarial networks. Adv. Energy Mater. 13 (2), 2202407. https://doi.org/10.1002/aenm.202202407.

- Dong, H., Blunt, M.J., 2009. Pore-network extraction from micro-computerized-tomography images. Phys. Rev. E 80 (3), 036307. https://doi.org/10.1103/physreve.80.036307.
- Dong, H., Sun, J., Golsanami, N., Cui, L., Jiang, L., Yan, G., Yan, W., Li, Y., 2018. A method to construct high-precision complex pore digital rock. J. Geophys. Eng. 15 (6), 2695–2703. https://doi.org/10.1088/1742-2140/aae04e.
- Dong, H., Sun, J., Arif, M., Zhang, Y., Yan, W., Iglauer, S., Golsanami, N., 2022. Digital rock-based investigation of conductivity mechanism in low-resistivity gas hydrate reservoirs: insights from the Muli area's gas hydrates. J. Petrol. Sci. Eng. 218, 110988. https://doi.org/10.1016/j.petrol.2022.110988.
- Dong, H., Zeng, X., Zhou, D., Zhu, J., Golsanami, N., Sun, J., Zhang, Y., 2023. Insights into the multiscale conductivity mechanism of marine shales from Wufeng—Longmaxi Formation in the southern Sichuan Basin of China. J. Energy Eng. 149 (3), 04023008. https://doi.org/10.1061/jleed9.eyeng-4667.
- Evstigneev, N.M., Ryabkov, O.I., Gerke, K.M., 2023. Stationary Stokes solver for single-phase flow in porous media: a blastingly fast solution based on Algebraic Multigrid Method using GPU. Adv. Water Resour. 171, 104340. https://doi.org/10.1016/j.advwatres.2022.104340.
- Fagbemi, S., Tahmasebi, P., Piri, M., 2018. Pore-scale modeling of multiphase flow through porous media under triaxial stress. Adv. Water Resour. 122, 206–216. https://doi.org/10.1016/j.advwatres.2018.10.018.
- Garboczi, E.J., 1998. Finite element and finite difference programs for computing the linear electric and elastic properties of digital images of random materials. NIST Interagency/Internal Report (NISTIR), National Institute of Standards and Technology, Gaithersburg, MD. https://doi.org/10.6028/nist.ir.6269.

 Golparvar, A., Zhou, Y., Wu, K., Ma, J., Yu, Z., 2018. A comprehensive review of pore
- Golparvar, A., Zhou, Y., Wu, K., Ma, J., Yu, Z., 2018. A comprehensive review of pore scale modeling methodologies for multiphase flow in porous media. Adv. Geo-Energy Res. 2 (4), 418–440. https://doi.org/10.26804/ager.2018.04.07.
- Goodfellow, I., Pouget-Abadie, J., Mirza, M., Xu, B., Warde-Farley, D., Ozair, S.,
 Bengio, Y., 2014. Generative adversarial nets. Adv. Neural Inf. Process. Syst. 27.
 Gulrajani, I., Ahmed, F., Arjovsky, M., Dumoulin, V., Courville, A.C., 2017. Improved training of wasserstein gans. Adv. Neural Inf. Process. Syst. 30.
- Hajizadeh, A., Safekordi, A., Farhadpour, F.A., 2011. A multiple-point statistics algorithm for 3D pore space reconstruction from 2D images. Adv. Water Resour. 34 (10), 1256–1267. https://doi.org/10.1016/j.advwatres.2011.06.003.
- Hazlett, R.D., 1997. Statistical characterization and stochastic modeling of pore networks in relation to fluid flow. Math. Geol. 29, 801–822. https://doi.org/ 10.1007/bf02768903.
- Karimpouli, S., Faraji, A., Balcewicz, M., Saenger, E.H., 2020. Computing heterogeneous core sample velocity using digital rock physics: a multiscale approach. Comput. Geosci. 135, 104378. https://doi.org/10.1016/j.cageo.2019.104378.
- Keehm, Y., Mukerji, T., Nur, A., 2004. Permeability prediction from thin sections: 3D reconstruction and Lattice-Boltzmann flow simulation. Geophys. Res. Lett. 31 (4), L04606. https://doi.org/10.1029/2003gl018761.
- Liu, M., Mukerji, T., 2022. Multiscale fusion of digital rock images based on deep generative adversarial networks. Geophys. Res. Lett. 49 (9), e2022GL098342. https://doi.org/10.1029/2022gl098342.
- Luo, X., Sun, J., Zhang, R., Chi, P., Cui, R., 2024. A multi-condition denoising diffusion probabilistic model controls the reconstruction of 3D digital rocks. Comput. Geosci. 184, 105541. https://doi.org/10.1016/j.cageo.2024.105541.
- Lv, X., Sun, J., Liao, B., Fang, C., Lv, K., Chen, Z., Wang, J., Sun, J., Chi, P., Sun, X., 2024. The effect of mixed wettability on flow characteristics in porous media of ultradeep gas reservoirs: molecular dynamics simulations and numerical simulations. Appl. Surf. Sci. 654, 159541. https://doi.org/10.1016/j.apsusc.2024.159541.
- Ma, Y., Liao, Q., Yan, Z., You, S., Song, X., Tian, S., Li, G., 2024. Stable diffusion for high-quality image reconstruction in digital rock analysis. Adv. Geo-Energy Res. 12 (3), 168–182. https://doi.org/10.46690/ager.2024.06.02.
- Mitchell, T.R., Roslin, A., Łaniewski-Wołłk, Ł., Onederra, I., Leonardi, C.R., 2023. Quantifying the permeability enhancement from blast-induced microfractures in porphyry rocks using a cumulant lattice Boltzmann method. Transport Porous Media 146 (3), 587–615. https://doi.org/10.1007/s11242-022-01875-4.
- Mosser, L., Dubrule, O., Blunt, M.J., 2017. Reconstruction of three-dimensional porous media using generative adversarial neural networks. Phys. Rev. E 96 (4), 043309. https://doi.org/10.1103/physreve.96.043309.
- Okabe, H., Blunt, M.J., 2004. Prediction of permeability for porous media reconstructed using multiple-point statistics. Phys. Rev. E 70 (6), 066135. https://doi.org/10.1103/physreve.70.066135.
- Qin, X., Xia, Y., Qiao, J., Chen, J., Zeng, J., Cai, J., 2024. Modeling of multiphase flow in low permeability porous media: effect of wettability and pore structure properties. J. Rock Mech. Geotech. 16 (4), 1127–1139. https://doi.org/10.1016/i.irmge.2023.06.007.
- Sun, J., Chi, P., Cheng, Z., Yang, L., Yan, W., Cui, L., 2021. A novel saturation calculation model of fractured-vuggy carbonate reservoir via multiscale pore networks: a case study from Sichuan Basin, China. J. Geophys. Eng. 18 (1), 85–97. https:// doi.org/10.1093/jge/gxaa071.
- Tahmasebi, P., Javadpour, F., Sahimi, M., 2015. Three-dimensional stochastic characterization of shale SEM images. Transport Porous Media 110, 521–531. https://doi.org/10.1007/s11242-015-0570-1.
- Tahmasebi, P., Sahimi, M., 2012. Reconstruction of three-dimensional porous media using a single thin section. Phys. Rev. E 85 (6), 066709. https://doi.org/10.1103/physreve.85.066709.
- Tian, H., Liu, L., Zhu, L., Ge, X., Ding, P., Cai, J., 2023. Relationship between

normalized permeability and resistivity index in hydrate-bearing sediments: fractal model and numerical simulation. Geophys. J. Int. 234 (1), 684–698. https://doi.org/10.1093/gji/ggad090.

- Wang, Y.D., Blunt, M.J., Armstrong, R.T., Mostaghimi, P., 2021. Deep learning in pore scale imaging and modeling. Earth Sci. Rev. 215, 103555. https://doi.org/ 10.1016/j.earscirev.2021.103555.
- Weibull, W., 1951. A statistical distribution function of wide applicability. J. Appl. Mech. 18 (3), 293–297. https://doi.org/10.1115/1.4010337.
- Wu, K., Van Dijke, M.I., Couples, G.D., Jiang, Z., Ma, J., Sorbie, K.S., Zhang, X., 2006. 3D stochastic modelling of heterogeneous porous media—applications to reservoir rocks. Transport Porous Media 65, 443–467. https://doi.org/10.1007/s11242-006-0006-z.
- Wu, Y., Tahmasebi, P., Lin, C., Zahid, M.A., Dong, C., Golab, A.N., Ren, L., 2019. A comprehensive study on geometric, topological and fractal characterizations of pore systems in low-permeability reservoirs based on SEM, MICP, NMR, and X-ray CT experiments. Mar. Petrol. Geol. 103, 12–28. https://doi.org/10.1016/ j.marpetgeo.2019.02.003.
- Wu, Y., Tahmasebi, P., Yu, H., Lin, C., Wu, H., Dong, C., 2020. Pore-scale 3D dynamic modeling and characterization of shale samples: considering the effects of

- thermal maturation. J. Geophys. Res. Solid Earth 125 (1), e2019JB018309. https://doi.org/10.1029/2019jb018309.
- Yan, W., Sun, J., Dong, H., Cui, L., 2021. Investigating NMR-based absolute and relative permeability models of sandstone using digital rock techniques. J. Petrol. Sci. Eng. 207, 109105. https://doi.org/10.1016/j.petrol.2021.109105.
- Yang, Y., Wang, K., Lv, Q., Askari, R., Mei, Q., Yao, J., Hou, J., Zhang, K., Li, A., Wang, C., 2021. Flow simulation considering adsorption boundary layer based on digital rock and finite element method. Pet. Sci. 18, 183—194. https://doi.org/10.1007/s12182-020-00476-4.
- Zhang, Y., Bijeljic, B., Gao, Y., Goodarzi, S., Foroughi, S., Blunt, M.J., 2023. Pore-scale observations of hydrogen trapping and migration in porous rock: demonstrating the effect of Ostwald ripening. Geophys. Res. Lett. 50 (7), e2022GL102383. https://doi.org/10.1029/2022gl102383.
- Zhu, L., Bijeljic, B., Blunt, M.J., 2024. Generation of heterogeneous pore-space images using improved pyramid Wasserstein generative adversarial networks. Adv. Water Resour. 190, 104748. https://doi.org/10.1016/j.advwatres.2024.104748.
- Zhu, L., Zhang, C., Zhang, C., Zhou, X., Zhang, Z., Nie, X., Liu, W., Zhu, B., 2019. Challenges and prospects of digital core-reconstruction research. Geofluids 2019 (1), 7814180. https://doi.org/10.1155/2019/7814180.